CrossMark

Mid-to-late M Dwarfs Lack Jupiter Analogs

Emily K. Pass[1] , Jennifer G. Winters[1,2] , David Charbonneau[1] , Jonathan M. Irwin[1,3], David W. Latham[1] , Perry Berlind[1],
Michael L. Calkins[1] , Gilbert A. Esquerdo[1] , and Jessica Mink[1]
[1] Center for Astrophysics | Harvard & Smithsonian, 60 Garden Street, Cambridge, MA 02138, USA
[2] Thompson Physics Lab, Williams College, 880 Main Street, Williamstown, MA 01267, USA
[3] Institute of Astronomy, University of Cambridge, Madingley Road, Cambridge CB3 0HA, UK; emily.pass@cfa.harvard.edu

Abstract

Cold Jovian planets play an important role in sculpting the dynamical environment in which inner terrestrial planets form. The core accretion model predicts that giant planets cannot form around low-mass M dwarfs, although this idea has been challenged by recent planet discoveries. Here, we investigate the occurrence rate of giant planets around low-mass (0.1–$0.3\,M_\odot$) M dwarfs. We monitor a volume-complete, inactive sample of 200 such stars located within 15 pc, collecting four high-resolution spectra of each M dwarf over six years and performing intensive follow-up monitoring of two candidate radial velocity variables. We use TRES on the 1.5 m telescope at the Fred Lawrence Whipple Observatory and CHIRON on the Cerro Tololo Inter-American Observatory 1.5 m telescope for our primary campaign, and MAROON-X on Gemini-North for high-precision follow up. We place a 95% confidence upper limit of 1.5% (68% confidence limit of 0.57%) on the occurrence of $M_P \sin i > 1\,M_J$ giant planets out to the water snow line and provide additional constraints on the giant planet population as a function of $M_P \sin i$ and period. Beyond the snow line ($100\ \mathrm{K} < T_{eq} < 150\ \mathrm{K}$), we place 95% confidence upper limits of 1.5%, 1.7%, and 4.4% (68% confidence limits of 0.58%, 0.66%, and 1.7%) for $3\,M_J < M_P \sin i < 10\,M_J$, $0.8\,M_J < M_P \sin i < 3\,M_J$, and $0.3\,M_J < M_P \sin i < 0.8\,M_J$ giant planets, respectively; i.e., Jupiter analogs are rare around low-mass M dwarfs. In contrast, surveys of Sun-like stars have found that their giant planets are most common at these Jupiter-like instellations.

Unified Astronomy Thesaurus concepts: Extrasolar gaseous giant planets (509); M dwarf stars (982); Radial velocity (1332); Surveys (1671); High resolution spectroscopy (2096)

Supporting material: machine-readable tables

1. Introduction

Recent work has shown that Jupiter-mass planets at Jovian instellations are a common occurrence around Sun-like stars, and the population peaks just beyond the snow line (Fulton et al. 2021; Rosenthal et al. 2022). But is the same true around much less massive stars? The core accretion theory predicts that giant planets are rare around M dwarfs, as giant planet formation within the gas dispersal time is inhibited by increasing dynamical time and decreasing mass surface density with decreasing stellar mass (Laughlin et al. 2004). In accordance with this prediction, only a handful of M dwarf giant planets have been identified by radial velocity (Marcy et al. 1998, 2001; Butler et al. 2006; Johnson et al. 2007, 2010; Bailey et al. 2009; Apps et al. 2010; Haghighipour et al. 2010; Howard et al. 2010a; Morales et al. 2019; Endl et al. 2022) and transit investigations (Johnson et al. 2012; Hartman et al. 2015; Bayliss et al. 2018; Bakos et al. 2020; Cañas et al. 2020, 2022; Gan et al. 2022; Jordán et al. 2022; Kanodia et al. 2022, 2023). Other such planets have been inferred through microlensing events (e.g., Kains et al. 2013; Mróz et al. 2017). However, individual detections are only anecdotal evidence. To measure occurrence rates, one must turn to surveys for which the sensitivity and completeness have been carefully investigated.

Various works have studied the occurrence rate of giant planets around M dwarfs, with each work reporting these rates in differing bins. Bonfils et al. (2013) determine an occurrence rate of <1% for $M_P \sin i = 100$–$1000\,M_\oplus$ planets with periods of 100–1000 days and 4^{+5}_{-1}% for periods of 1000–10,000 days. Montet et al. (2014) report a $6.5\% \pm 3.0\%$ occurrence rate for $1\,M_J < M_P < 13\,M_J$ planets out to 20 au. Sabotta et al. (2021) find an occurrence rate of 6^{+4}_{-3}% for $M_P \sin i = 100$–$1000\,M_\oplus$ planets with periods of up to 1000 days. Combining the Bonfils et al. (2013) radial velocity and Gould et al. (2010) microlensing results, Clanton & Gaudi (2014a) measure an occurrence rate of $2.9^{+1.3}_{-1.5}$% for $1\,M_J < M_P \sin i < 13\,M_J$ planets with $1 < P < 10^4$ day periods around M dwarfs, making Jupiter-size planets 4.3 times rarer around M dwarfs than around FGK stars. However, the definition of M dwarfs is broad, spanning nearly an order of magnitude in stellar mass (0.08–$0.62\,M_\odot$; Benedict et al. 2016). Extant occurrence rate constraints are based on samples dominated by the higher-mass end; for example, Gould et al. (2010) report that their lens distribution is centered at $M_* = 0.5\,M_\odot$, while the mean stellar mass in the Bonfils et al. (2013) sample is $0.35\,M_\odot$. Given the stellar mass dependence of the factors opposing giant planet formation around M dwarfs, low-mass M dwarfs are best suited to probing tensions with the core formation theory.

Only two of the known M dwarf giant planets orbit $M_* \lesssim 0.3\,M_\odot$ stars: LHS 252 b, a $0.46\,M_J$ planet with a 204 day period (Morales et al. 2019), and GJ 83.1 b, a $0.21\,M_J$ planet with a 771 day period (Feng et al. 2020; Quirrenbach et al. 2022). An additional candidate has been proposed by Curiel et al. (2020): TVLM 513-46 b, a $0.4\,M_J$ planet with a
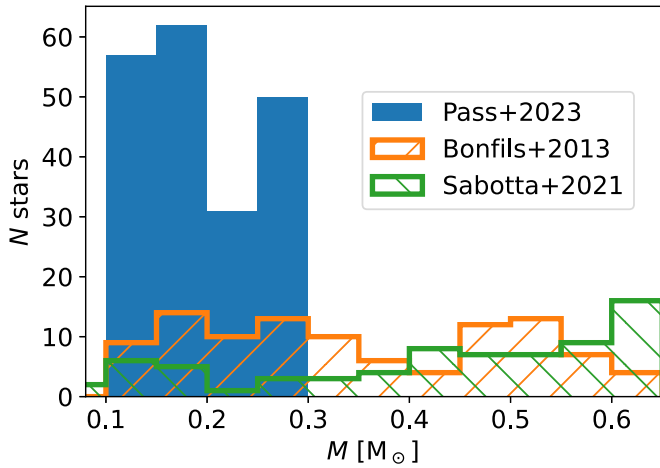
Figure 1. The mass distribution of our stars. We contrast this sample with Bonfils et al. (2013; B13), the largest radial velocity survey of M dwarfs in the literature, as well as Sabotta et al. (2021; S21)'s recent results from the CARMENES survey. Previous studies of giant planets around M dwarfs have been dominated by early Ms, with masses that are not so dissimilar to those of Sun-like stars. More poorly studied are low-mass, fully convective M dwarfs. Our sample is volume complete and contains 200 such stars with masses of 0.1–0.3 $M_\odot$. Previous studies have dramatically smaller samples over this mass range (46 in B13 and 15 in S21) and are not volume complete. Note that this figure compares total sample size; for a comparison of effective sample size as a function of planetary mass and period, an interested reader may compare our Figure 3 with Figure 15 of B13 and Figure 3 of S21.

221 day period. 2MA J1227-7227 b, a young 0.85 R_J planet with a 27.4 day period, may be an additional such object, although Mann et al. (2022) suggest that it will eventually contract into a sub-Neptune. The directly imaged planet 2MA J0437+2651 b has also been interpreted as a super-Jupiter around a young 0.15–0.18 $M_\odot$ star (Gaidos et al. 2022). Despite this small sample, tension with core accretion theory is already emerging, as Morales et al. (2019) find that the properties of LHS 252 b cannot be reproduced through existing core accretion models. The authors suggest formation via gravitational instability (Boss 2006) as a possible alternative. These tensions are further discussed in Schlecker et al. (2022).

Previous radial velocity studies investigating the occurrence rate of giant planets around M dwarfs have included too few low-mass M dwarfs to constrain the occurrence rate of giant planets in this population robustly (Figure 1; for consistency in comparing between studies, we calculate all masses in this figure using Gaia parallaxes and the K-band mass–luminosity relation from Benedict et al. 2016). Using a small sample of 23 M dwarfs less massive than 0.34 $M_\odot$, Sabotta et al. (2021) estimate an occurrence rate of $16\%^{+15\%}_{-9\%}$ for planets with $M_P \sin i = 100$–$1000\,M_\oplus$ at periods of 100–1000 days, which could indicate an enhanced rate of giant planet formation around low-mass M dwarfs; however, they note that selection biases in this sample may result in this value being overestimated by up to a factor of five. A large, statistically robust sample is necessary to establish whether planets like LHS 252 b are rare oddities, or whether the core accretion framework is fundamentally inaccurate for low-mass M dwarfs.

In addition to informing planet formation theories, the occurrence rate of giant planets is relevant to questions of the formation of terrestrial planets, their accretion of material from beyond the snow line, and ultimately their habitability. Due to their strong gravities, giant planets set the dynamical and collisional conditions under which terrestrial planets form

(Lunine 2001). A cold Jupiter may be necessary to create a planetary system like our own, playing a role in preventing the inward migration of gas giant cores (Izidoro et al. 2015; Kruijer et al. 2017) and setting the water budget of the terrestrial planets (Raymond & Izidoro 2017; Bitsch et al. 2021). As nearby M dwarfs represent the most favorable hosts for the detection and characterization of Earth-like planets with present and near-future instrumentation (Charbonneau & Deming 2007; Snellen et al. 2013; Morley et al. 2017; López-Morales et al. 2019), the occurrence of giant planets around the lowest-mass stars is relevant for evaluating the habitability of the systems that can be studied in detail in the foreseeable future.

In Section 2, we present our spectroscopic survey of nearby 0.10–0.30 $M_\odot$ M dwarfs. Section 3 describes our data reduction process, radial velocity calculations, and error estimates. In Section 4, we discuss our identification and follow up of radial velocity variables and our calculation of occurrence rate constraints. We present a discussion and comparison to the literature in Section 5 and a summary in Section 6.

2. Stellar Sample and Data Collection

This work is part of a series of papers presenting the results of the volume-complete spectroscopic survey of 0.10–0.30 $M_\odot$ M dwarfs within 15 pc, defined in Winters et al. (2021). The sample totals 413 stars and excludes M dwarfs that are close companions (separations $< 4''$) to more massive primaries, as the spectra would be strongly contaminated by the brighter star. Between 2016 and 2022, we collected four high-resolution spectra of each of these 413 stars using the Tillinghast Reflector Echelle Spectrograph (TRES; $R = 44{,}000$) at the 1.5 m telescope at the Fred Lawrence Whipple Observatory for sources with $\delta > -15°$ and the CTIO HIgh ResolutiON (CHIRON; $R = 80{,}000$) spectrograph at the Cerro Tololo Inter-American Observatory 1.5 m telescope for sources with $\delta < -15°$. Exposure times were selected based on a target per-pixel signal-to-noise ratio (S/N) of 15 in the TiO bands around 7100 Å, ranging from 60 to 5400 s; however, in practice our observations span a range of S/Ns, with a typical value of 11 for our TRES observations and 8 for our CHIRON observations. Forthcoming entries in this series will discuss the active subsample, the binary subsample, and present galactic kinematics for all stars (Pass et al. 2023; J. G. Winters et al. 2023, in preparation).

In this work, we consider only the single, inactive subsample, as with four observations per star, we cannot easily distinguish variations due to an orbiting planet from other sources of variation. As we perform intensive follow-up vetting of each candidate flagged as potentially variable from our four-observation campaign, selecting the single, inactive subsample allows us to minimize the time spent intensively monitoring candidates that are ultimately false positives. We discard all binaries separated by less than $4''$, as light from both stars would fall in the spectroscopic aperture under typical seeing. To avoid a large number of false positives due to activity-induced radial velocity variability (e.g., Tal-Or et al. 2018), we neglect active stars for which we measure Hα emission stronger than a median equivalent width (EW) of −1 Å using the method of Medina et al. (2020). We use the notation that a negative EW indicates emission. This −1 Å threshold has been used to distinguish between active and inactive M dwarfs in previous work such as Newton et al. (2017). Of the stars without close binaries, we classify 123 as active based on this

criterion; this group includes the known giant planet hosts GJ 83.1 (Hα EW = −2.3 Å) and LHS 252 (Hα EW = −1.8 Å). While "inactive" M dwarfs may still have activity-induced variability that masquerades as a planet (e.g., Lubin et al. 2021), this phenomenon is less ubiquitous and can be evaluated on a case-by-case basis through intensive follow up of the small number of inactive candidates. After making these cuts, 200 M dwarfs remain in our sample (Figure 1), of which we observe 122 with TRES and 78 with CHIRON.

3. Data Reduction

3.1. Radial Velocities

We extract the spectra using the standard TRES (Buchhave et al. 2010) and CHIRON (Tokovinin et al. 2013) pipelines and measure radial velocities using an updated version of the method presented in Winters et al. (2020), which itself is based on Kurtz & Mink (1998). In addition to utilizing the TiO bandhead features from 7065 to 7165 Å (TRES echelle order 41 and CHIRON echelle order 44), we also consider five additional red echelle orders—36, 38, 39, 43, and 45 for TRES and 36, 37, 39, 40, and 51 for CHIRON, which represent wavelengths with low telluric contamination and high information content for low-mass M dwarfs. These orders fall within 6400–7850 Å.

We obtain an initial radial velocity estimate for each spectrum by cross-correlating with a template of Barnard's Star in the manner described in Winters et al. (2020). This method also produces an estimate of $v \sin i$. We then shift and stack our observations to create a high-S/N template spectrum of the average slowly rotating, low-mass M dwarf observed by TRES. To stack the observations, we first create an error-weighted mean spectrum for each star. We then median combine the spectra of all 122 stars that were observed with TRES. Prior to coaddition, we mask regions with telluric depths greater than 2% in a representative TAPAS spectrum (Bertaux et al. 2014) or skyline emission greater than 5×10^{-17} erg s^{-1} cm^{-2} Å^{-1} in the UVES sky emission atlas (Hanuschik 2003). Our final template neglects wavelengths at the edges of orders that do not include information from at least ten M dwarfs.

In creating this average low-mass M dwarf template, we note that the information content Q (Bouchy et al. 2001) in TRES echelle order 45 differs by a factor of two across our sample, with the highest values obtained for cold, metal-rich stars and the lowest values obtained for hot, metal-poor stars. To minimize radial velocity uncertainties caused by template mismatch, we therefore create six different average templates for TRES. Each star is initially classified by the Q we measure in order 45, dividing the sample equally into six preliminary bins. We then reclassify each star by determining the preliminary template that maximizes the cross-correlation coefficient, recreating the templates based on these refined classifications, and repeating until the classifications converge. This iterative process prevents stars from being misclassified in cases where their Q is not representative of their spectral type (for example, when noise leads to inflated estimates of Q). We perform a similar analysis for CHIRON, although we create only three templates so that we attain an acceptable S/N given the smaller number of observations available for coaddition.

We compute the cross-correlation function as the weighted sum:

$$r_j = \frac{\sum_i a_{i+j} b_i w_{i+j}}{\sqrt{\left(\sum_i a_{i+j}^2 w_{i+j}\right)\left(\sum_i b_i^2 w_{i+j}\right)}}, \qquad (1)$$

where a is the observed flux, b is the template flux, and w are the variance weights (or $w_i = 0$ for masked telluric or skyline features). This sum is evaluated jointly across the six echelle orders. Both a and b are blaze corrected, normalized, continuum subtracted, and oversampled by a factor of 32. Our code also includes the ability to broaden b rotationally to analyze rapidly rotating stars, but there are no such stars in this study due to our Hα activity cut. The errors used to calculate w consider photon noise and read noise in a, and are scaled based on the blaze correction.

Lastly, we determine the radial velocity shift by fitting a Lorentzian to the cross-correlation peak.

3.2. Uncertainties

We calculate theoretical radial velocity uncertainties using the equation derived in Bouchy et al. (2001):

$$\frac{\delta_{RV}}{c} = \frac{1}{\sqrt{\sum_i \lambda_i^2 (\partial b_i / \partial \lambda_i)^2 w_i}}, \qquad (2)$$

where b is once again the template flux and w are the variance weights. In the photon-noise limit, this equation simplifies to $\delta_{RV} = c/(Q \times S/N)$.

Alternatively, we can estimate the radial velocity uncertainty directly from the cross-correlation function using the equation from Zucker (2003):

$$\frac{\delta_{RV}}{c} = \sqrt{-\left(N_{eff} \frac{r''_{max}}{r_{max}} \frac{r_{max}^2}{1 - r_{max}^2}\right)^{-1}}, \qquad (3)$$

where we have replaced N with $N_{eff} \equiv (\sum_i w_i)^2 / \sum_i w_i^2$ to account for our error weighting. In this equation, r_{max} denotes the cross-correlation peak and r''_{max} represents its second derivative.

Generally, we find good agreement between these two uncertainty estimators, although they differ when template mismatch is a significant source of uncertainty (e.g., in the high-S/N limit or when there is substantial rotational broadening, although the latter is not relevant for the sample discussed here). We make the conservative choice to always adopt the larger of the two.

To validate our uncertainties, we also compute the cross-correlation function for each of the six echelle orders individually and compare the resultant radial velocities using the chi-squared estimator:

$$\chi^2 = \sum_{k=1}^{6} w_k (v_{rad,k} - v_{rad})^2, \qquad (4)$$

where the variance weights ($w_k = 1/\delta_k^2$) are determined using the above uncertainty calculations for each order. For both TRES and CHIRON, the resulting distribution of χ^2 across all observations shows good agreement with a chi-squared

Table 1
First Five Lines of the Online, Machine-readable Table Listing our Radial Velocity (RV) Measurements and Their Uncertainties

Name	Inst	BJD −2,457,640 (day)				Relative RV (m s^{-1})				RV Error (m s^{-1})				$P(\chi^2)$
		1	2	3	4	1	2	3	4	1	2	3	4	
GJ 1001	C	689.8474	1067.8194	1083.7259	1545.6148	28	6	−17	−16	20	33	22	20	0.343
GJ 1002	T	293.9686	466.6685	469.5924	1049.9704	18	−8	8	−24	29	98	31	29	0.761
LEP 0011+5908	T	122.6580	476.6877	1102.8183	1856.7702	4	−6	−28	28	21	25	36	35	0.723
GJ 12	T	34.7181	280.9609	1014.9527	1828.8724	36	13	−33	−24	35	29	40	31	0.468
GJ 15B	T	1.9447	301.9763	1009.9604	1851.8027	−26	−16	5	62	20	26	29	27	0.063

Note. In the instrument column, T denotes TRES and C denotes CHIRON.

(This table is available in its entirety in machine-readable form.)

distribution with five degrees of freedom, as we would expect for properly estimated uncertainties.

An independent source of uncertainty comes from the barycentric correction, which ideally would be calculated at the photon-weighted midpoint of the observation. As we lack information on the temporal flux distribution over an exposure, we adopt the geometric midpoint as the observation time. This approximation can produce a systematic error of up to 2 m s^{-1} per minute of difference between the geometric and photon-weighted midpoints, as shown in Tronsgaard et al. (2019; see their Equation (8)). That work found that the offset between these midpoints is typically around 5% of the exposure length. For completeness, we therefore add a radial velocity uncertainty term in quadrature corresponding to a 5% offset to the midpoint time; however, we find that this contribution is ultimately negligible in the total error budget.

We note that our uncertainty estimates thus far do not account for the long-term instability of the spectrograph. Over the observation campaign, one zero-point offset occurred for CHIRON and two for TRES due to hardware and software changes to the instrument. To determine the amplitudes of these offsets, we create an ensemble of all our observations from each spectrograph, subtracting the error-weighted mean radial velocity of each star to put the observations on a common zero-point. We then use these ensembles to measure the amplitude of the radial velocity discontinuities and apply a correction to subsequent measurements. For CHIRON, this offset is +50 m s^{-1} at BJD = 2,458,840 days. For TRES, these offsets are +45 m s^{-1} at BJD = 2,458,700 days and −20 m s^{-1} at BJD = 2,459,218 days.

To evaluate the stability of each spectrograph outside of these events, we consider the standard deviation of the most precise observations—namely, observations with uncertainty estimates between 5 and 18 m s^{-1}. If our observations were unaffected by a noise floor, we would expect the standard deviation to fall somewhere within this 5–18 m s^{-1} range. Note that the delta degrees of freedom (ddof) in this calculation is not 1; this would underestimate the standard deviation, as we have subtracted the error-weighted mean of each star. The ddof is also not equal to the number of stars; this would overestimate the standard deviation, as all observations are used to inform the error-weighted means, not just observations with small estimated uncertainties. We make a more reasonable estimate of the ddof by assuming that each star contributes $\sum w_j / \sum w_i$, where w_j are the variance weights of the observations with estimated uncertainties below 18 m s^{-1} and w_i are the variance weights of all observations. The maximum value of this expression is 1, which occurs when the error-weighted mean radial velocity is fully informed by observations with small

estimated uncertainties. For CHIRON, our calculation includes 137 observations, has ddof = 47.4, and results in a standard deviation of 20 m s^{-1}. For TRES, we have 48 observations with small estimated uncertainties, ddof = 16.2, and a standard deviation of 21 m s^{-1}. As these results are greater than 18 m s^{-1}, it appears that instrumental instability is indeed setting a noise floor. These results are consistent with Winters et al. (2020), who found typical rms velocity residuals of 20 m s^{-1} using orbital solutions for bright, slowly rotating low-mass M dwarf binaries observed by TRES. As uncertainties below 20 m s^{-1} may therefore be underestimated due to instrumental instability, we do not allow our estimates to be smaller than this floor.

Our radial velocity measurements and uncertainties for all 200 stars are available in a machine-readable format, with the format of this file shown in Table 1.

4. Data Analysis

4.1. Identification and Follow Up of Candidate Variables

We use the metric $P(\chi^2)$ to evaluate whether each radial velocity time series is consistent with an unvarying model given the uncertainties determined in the previous section. In this context, the chi-squared estimator is given by:

$$\chi^2 = \sum_{i=1}^{4} \frac{(v_{\mathrm{rad},i} - \langle v_{\mathrm{rad}} \rangle)^2}{\delta_{\mathrm{RV},i}^2}, \qquad (5)$$

with $N_{\mathrm{obs}} - 1 = 3$ degrees of freedom. $\langle v_{\mathrm{rad}} \rangle$ denotes the error-weighted mean of the radial velocity time series. We flag a signal as significant if the variability is inconsistent with the null hypothesis with 99% confidence ($P(\chi^2) < 1\%$). In other words, we are searching for statistically significant excess radial velocity jitter; if such jitter is detected, further follow up is necessary to verify that this jitter is due to a planet and not an astrophysical or statistical false positive. Given our sample size of 200 stars, we expect an average of two statistical false positives due to random chance.

We conducted a preliminary analysis of our data in early 2021, from which we identified two stars—LHS 2899 and G 125-34— as candidate variables based on this $P(\chi^2) < 1\%$ cut. Based on the significance of the variability in the initial four observations, we proceeded to collect an additional 41 observations of LHS 2899 and 46 observations of G 125-34 with TRES between 2021 April and 2022 May. At the time of the preliminary analysis, we had yet to obtain a fourth observation for some stars in the sample; our follow up of LHS 2899 and G 125-34 therefore occurred concurrently with our main observation campaign, which was completed on 2022 May 11. When analyzing

Table 2
Stellar Properties and Radial Velocity Variability for Our 200 Stars

Name	2MASS ID	M_* $(M_\odot)$	L_* $(L_\odot)$	$P(\chi^2)$	Name	2MASS ID	M_* $(M_\odot)$	L_* $(L_\odot)$	$P(\chi^2)$
GJ 1001	00043643-4044020	0.262	0.0079	0.343	LHS 2385	11163766-2757186	0.186	0.0045	0.013
GJ 1002	00064325-0732147	0.115	0.0015	0.761	LHS 2395	11193058+4641437	0.112	0.0014	0.547
LEP 0011+5908	00113182+5908400	0.107	0.0012	0.723	LHS 2415	11285624+1010395	0.286	0.0091	0.929
GJ 12	00154919+1333218	0.249	0.0075	0.468	LHS 306	11310835-1457201	0.157	0.0035	0.078
GJ 15B	00182549+4401376	0.157	0.0034	0.063	SCR 1138-7721	11381671-7721484	0.118	0.0017	0.291
LHS 112	00202922+3305081	0.119	0.0016	0.706	SIP 1141-3624	11412152-3624346	0.173	0.0041	0.322
GJ 1013	00313539-0552115	0.275	0.0088	0.250	GJ 442B	11463269-4029476	0.164	0.0037	0.055
L 291-115	00331349-4733165	0.126	0.0020	0.667	GJ 445	11474143+7841283	0.252	0.0076	0.495
GJ 1014	00355557+1028352	0.132	0.0024	0.022	GJ 447	11474440+0048164	0.173	0.0041	0.593
LHS 1134	00432603-4117337	0.210	0.0057	0.175	GJ 1151	11505787+4822395	0.164	0.0038	0.122
LHS 1140	00445930-1516166	0.179	0.0044	0.619	L 758-107B	12111697-1958213	0.272	0.0085	0.577
GDR 20049+6518	00492565+6518038	0.140	0.0028	0.609	GJ 465	12245243-1814303	0.274	0.0092	0.480
GJ 1025	01005643-0426561	0.198	0.0051	0.763	GJ 1158	12293453-5559371	0.233	0.0066	0.845
GJ 1028	01045368-1807292	0.136	0.0025	0.683	LHS 337	12384914-3822527	0.152	0.0033	0.712
GJ 1031	01081826-2848207	0.207	0.0055	0.478	LHS 2597	12393641-2658111	0.114	0.0015	0.621
GJ 1035	01195227+8409327	0.155	0.0034	0.686	GJ 480.1	12404633-4333595	0.185	0.0047	0.737
GJ 61B	01365042+4123325	0.187	0.0047	0.166	LHS 2608	12421964-7138202	0.242	0.0071	0.395
LP 991-84	01392170-3936088	0.133	0.0023	0.449	LHS 2674a	13065025+3050549	0.133	0.0023	0.384
LHS 5045	01525159-4805413	0.217	0.0061	0.611	LHS 2718	13200391-3524437	0.259	0.0079	0.151
L 173-19	02003830-5558047	0.275	0.0086	0.461	LHS 350	13225673+2428034	0.265	0.0080	0.442
LHS 1326	02021620+1020136	0.112	0.0013	0.092	GJ 1171	13303106+1909340	0.146	0.0031	0.728
LHS 1339	02054859-3010361	0.206	0.0057	0.154	LHS 2784	13424328+3317255	0.281	0.0088	0.203
GJ 105B	02361535+0652191	0.263	0.0079	0.035	LP 911-56	13464607-3149258	0.104	0.0009	0.400
GJ 1050	02395066-3407557	0.287	0.0097	0.620	GJ 1179A	13481341+2336486	0.122	0.0019	0.807
SCR 0246-7024	02460224-7024062	0.137	0.0026	0.675	LTT 5437	13571306-2922252	0.279	0.0091	0.101
LHS 1443	02463486+1625115	0.101	0.0009	0.724	SSS 1358-3938	13580529-3937545	0.129	0.0023	0.713
LP 831-1	02543950-2215584	0.246	0.0074	0.540	LHS 2830	13581392+1234438	0.220	0.0061	0.780
LHS 1481	02581021-1253066	0.184	0.0048	0.731	G 165-58	14155637+3616368	0.241	0.0071	0.351
LTT 1445A	03015142-1635356	0.258	0.0080	0.956	GJ 545	14200739-0937127	0.263	0.0079	0.036
LHS 1490	03020638-3950516	0.111	0.0014	0.993	LHS 2899	14211512-0107199	0.237	0.0067	0.030
GJ 1055	03090015+1001257	0.133	0.0024	0.095	LEP 1422-7023	14221943-7023371	0.121	0.0019	0.541
GJ 1053	03105861+7346189	0.128	0.0023	0.028	LEP 1455+3006	14551146+3006454	0.170	0.0040	0.914
GJ 1057	03132299+0446293	0.160	0.0035	0.632	GJ 2112	15221293-2749436	0.180	0.0043	0.356
LHS 1516	03141241+2840411	0.108	0.0012	0.640	GJ 585	15235112+1727569	0.171	0.0041	0.560
GJ 1059	03230175+4200269	0.124	0.0021	0.419	GJ 589B	15352039+1743045	0.129	0.0023	0.586
LHS 176	03353849-0829223	0.119	0.0017	0.725	GJ 589A	15352059+1742470	0.296	0.0103	0.961
GJ 1061	03355969-4430453	0.123	0.0019	0.946	GJ 590	15363450-3754223	0.211	0.0056	0.460
L 228-92	03385590-5234107	0.146	0.0031	0.257	GJ 1194A	15400352+4329396	0.295	0.0103	0.486
LHS 1593	03472091+0841464	0.134	0.0025	0.283	GJ 1194B	15400374+4329355	0.204	0.0050	0.962
GJ 1065	03504432-0605400	0.198	0.0051	0.614	GJ 609	16025098+2035218	0.250	0.0074	0.727
LP 357-56	03544620+2416246	0.116	0.0013	0.746	GJ 611B	16045093+3909359	0.145	0.0029	0.115
2MA0406-0534	04060688-0534444	0.224	0.0061	0.164	GJ 618B	16200321-3731485	0.164	0.0034	0.079
LHS 1629	04063732+7916012	0.134	0.0024	0.242	LHS 3241	16463154+3434554	0.108	0.0011	0.928
GJ 1068	04102815-5336078	0.129	0.0023	0.597	LP 154-205	16475517-6509116	0.168	0.0039	0.355
GJ 1072	04505083+2207224	0.139	0.0026	0.499	GJ 643D	16552527-0819207	0.210	0.0056	0.226
GJ 1073	04523448+4042255	0.212	0.0057	0.935	LHS 3262	17032384+5124219	0.180	0.0044	0.641
LHS 1723	05015746-0656459	0.166	0.0039	0.931	GJ 1214A	17151894+0457496	0.178	0.0042	0.828
LHS 1731	05032009-1722245	0.290	0.0097	0.798	GJ 1220	17311725+8205198	0.158	0.0035	0.494
UPM 0505+4414	05050591+4414037	0.145	0.0030	0.630	LHS 3324	17460465+2439049	0.278	0.0092	0.919
G 86-28	05103956+2946479	0.261	0.0082	0.858	GJ 693	17463427-5719081	0.280	0.0092	0.413
LEHPM 2-1009	05273058-5129158	0.129	0.0022	0.195	BARNARDS	17574849+0441405	0.155	0.0033	0.168
GJ 203	05280015+0938382	0.231	0.0065	0.089	GJ 1223	18024624+3731048	0.139	0.0027	0.579
LHS 5108	05325194+3349474	0.202	0.0053	0.471	LP 449-10	18064856+1720472	0.196	0.0051	0.951
GJ 213	05420897+1229252	0.221	0.0061	0.243	G 140-51	18163154+0452456	0.174	0.0040	0.066
GJ 2045	05421271-0527567	0.122	0.0019	0.712	LHS 461B	18180345+3846359	0.165	0.0038	0.904
LEP 0556+1144	05565722+1144333	0.125	0.0020	0.597	GJ 712	18220671+0620376	0.294	0.0100	0.244
LHS 1805	06011106+5935508	0.275	0.0085	0.470	GJ 1227	18222719+6203025	0.162	0.0037	0.022
LHS 1809	06022918+4951561	0.134	0.0024	0.693	SCR 1841-4347	18410977-4347327	0.111	0.0013	0.398
GJ 1088	06105288+4324178	0.296	0.0097	0.088	GJ 1230B	18410981+2447195	0.195	0.0042	0.069
G 192-22	06140240+5140081	0.264	0.0083	0.667	LP 867-15	18421107-2328582	0.259	0.0081	0.262
LP 779-34	06151198-1626152	0.190	0.0049	0.067	GJ 725B	18424688+5937374	0.265	0.0084	0.470
L 308-57	06210665-4905379	0.172	0.0040	0.301	LHS 5341	18430697-5436481	0.240	0.0071	0.033
GJ 232	06244132+2325585	0.152	0.0032	0.482	G 184-31	18495449+1840295	0.162	0.0037	0.497

Table 2
(Continued)

Name	2MASS ID	M_* ($M_\odot$)	L_* ($L_\odot$)	$P(\chi^2)$	Name	2MASS ID	M_* ($M_\odot$)	L_* ($L_\odot$)	$P(\chi^2)$
SCR 0642-6707	06422703-6707193	0.110	0.0013	0.731	GJ 732A	18533991-3836442	0.289	0.0093	0.368
GJ 1092	06490542+3706533	0.177	0.0042	0.027	GJ 1232	19095098+1740074	0.189	0.0049	0.077
GJ 1093	06592868+1920577	0.123	0.0018	0.822	LEP 1916+8413	19162483+8413411	0.150	0.0031	0.256
G 107-48	07073776+4841138	0.163	0.0037	0.720	GJ 754.1B	19203346-0739435	0.259	0.0087	0.187
L 136-37	07205204-6210118	0.265	0.0083	0.946	GJ 754	19204795-4533283	0.175	0.0042	0.022
SCR 0736-3024	07365666-3024160	0.196	0.0051	0.535	LHS 475	19205439-8233170	0.275	0.0085	0.107
GJ 283B	07401922-1724449	0.101	0.0008	0.737	GJ 1235	19213867+2052028	0.194	0.0050	0.084
LHS 1950	07515138+0532572	0.154	0.0034	0.255	GJ 1236	19220206+0702310	0.223	0.0064	0.066
GJ 1103	07515465-0000117	0.192	0.0049	0.176	GJ 1238	19241634+7533121	0.121	0.0018	0.073
GJ 1105	07581269+4118134	0.284	0.0090	0.653	G 125-34	19484080+3555178	0.237	0.0067	0.008
GJ 299	08115757+0846220	0.138	0.0027	0.428	GJ 770C	19542064-2356398	0.166	0.0036	0.719
GJ 300	08124088-2133056	0.282	0.0091	0.117	GJ 1248	20035098+0559440	0.267	0.0090	0.332
LHS 2025	08313011+7303459	0.279	0.0088	0.620	GJ 774B	20040195-6535586	0.220	0.0062	0.858
GJ 2070	08342587-0108391	0.246	0.0074	0.103	GJ 1253	20260528+5834224	0.158	0.0034	0.321
LEP 0840+3127	08401597+3127068	0.299	0.0098	0.130	GJ 1251	20280382-7640164	0.169	0.0039	0.979
LEP 0844-4805	08443891-4805218	0.200	0.0053	0.148	GJ 1256	20403364+1529572	0.189	0.0048	0.096
GJ 324B	08524084+2818589	0.278	0.0089	0.957	LP 816-60	20523304-1658289	0.238	0.0069	0.743
LHS 2088	08595604+7257364	0.158	0.0035	0.573	LHS 3593	20533304+1037020	0.180	0.0044	0.014
LP 60-179	09025284+6803464	0.265	0.0081	0.038	GJ 810B	20553706-1403545	0.140	0.0028	0.078
GJ 1123	09170532-7749233	0.224	0.0063	0.686	GJ 2151	21031390-5657479	0.242	0.0071	0.751
LEP 0921-0219	09214812-0219433	0.272	0.0090	0.679	LEP 2124+4003	21243234+4003599	0.130	0.0022	0.660
GJ 359	09410199+2201291	0.145	0.0030	0.782	LHS 510	21304763-4042290	0.205	0.0053	0.445
GJ 1128	09424635-6853060	0.176	0.0043	0.258	WT 795	21362532-4401005	0.197	0.0052	0.162
LHS 5156	09424960-6337560	0.210	0.0057	0.788	LHS 512	21384369-3339555	0.280	0.0088	0.075
LHS 272	09434633-1747066	0.154	0.0036	0.478	LEP 2146+3813	21462206+3813047	0.178	0.0043	0.093
GJ 1129	09444731-1812489	0.299	0.0099	0.318	LP 698-42	21471744-0444406	0.157	0.0035	0.539
LHS 2224	10092996+5117197	0.181	0.0044	0.831	LHS 516	21565513-0154100	0.144	0.0030	0.060
GJ 1132	10145184-4709244	0.192	0.0049	0.765	LHS 3746	22022935-3704512	0.251	0.0074	0.275
LEP 1015+1729	10155390+1729271	0.287	0.0091	0.367	GJ 1265	22134277-1741081	0.168	0.0040	0.699
LEHPM 2-2758	10384782-8632441	0.252	0.0075	0.097	GJ 1270	22294885+4128479	0.259	0.0078	0.381
GJ 1134	10413809+3736397	0.205	0.0054	0.408	L 645-74B	22382544-2921244	0.254	0.0076	0.066
LHS 288	10442131-6112384	0.106	0.0012	0.959	LHS 3844	22415815-6910089	0.151	0.0031	0.496
LHS 2303	10442927-1838063	0.125	0.0021	0.853	GJ 1277	22562466-6003490	0.172	0.0040	0.573
LHS 2310	10473868-7927458	0.251	0.0075	0.605	LEHPM 2-2163	23303802-8455189	0.138	0.0027	0.240
GJ 402	10505201+0648292	0.282	0.0091	0.056	GJ 1286	23351050-0223214	0.118	0.0017	0.160
GJ 403	10520440+1359509	0.278	0.0087	0.164	LHS 547	23365227-3628518	0.171	0.0040	0.968
LHS 296	11011965+0300171	0.164	0.0037	0.692	GJ 905	23415498+4410407	0.140	0.0026	0.125

(This table is available in machine-readable form.)

observations of all stars after data collection was completed, we found that the stability of the TRES zero-point worsened in 2021–2022, motivating us to augment our 20 m s^{-1} noise floor with a dynamic floor using the radial velocity jitter in the TRES standard stars over each observing run (S. Quinn, private communication). These standards are quiet, Sun-like stars that are known to have very low intrinsic radial velocity variation based on observations from more precise instruments. We use these standards to determine the rms scatter in each observing run, which we add to our uncertainties in quadrature. In theory, we should also be able to correct for zero-point offsets using these standards; however, they are Sun-like stars and analyzed in bluer orders than our M dwarf spectra, and we find that the offsets in the M dwarfs are not entirely commensurate with those seen in the standards.

With this refinement to our uncertainty estimation, the $P(\chi^2)$ in the initial four observations of LHS 2899 increased from <1% to 3%, no longer meeting our follow-up criterion. For the purposes of our statistical study, it is therefore not necessary to establish whether the variability of LHS 2899 is a planet or a false positive; however, for completeness we will nonetheless discuss it here. G 125-34 retained its $P(\chi^2) < 1\%$ designation and no other signals became significant with this change. $P(\chi^2)$ values for all stars are given in Table 2.

For both G 125-34 and LHS 2899, the significance of the candidate variability increased with the TRES follow-up observations, with a final $P(\chi^2) = 4.3 \times 10^{-5}$ for G 125-34 and $P(\chi^2) = 1.0 \times 10^{-5}$ for LHS 2899. A periodogram analysis yielded candidate periods for orbital solutions, although the precision and quantity of the data were insufficient to prove or disprove the presence of a planet definitively. The preferred planetary solutions were a 0.22 M_J planet on a 77 day orbit for G 125-34 and a 0.70 M_J planet on a 337 day orbit for LHS 2899.

To reach definitive conclusions about the dispositions of these candidates, we obtained five observations of LHS 2899 and 13 observations of G 125-34 using the MAROON-X spectrograph (Seifahrt et al. 2018), an extreme precision radial velocity instrument on the 8.1 m Gemini-North telescope, over a two month interval. These observations were reduced by the
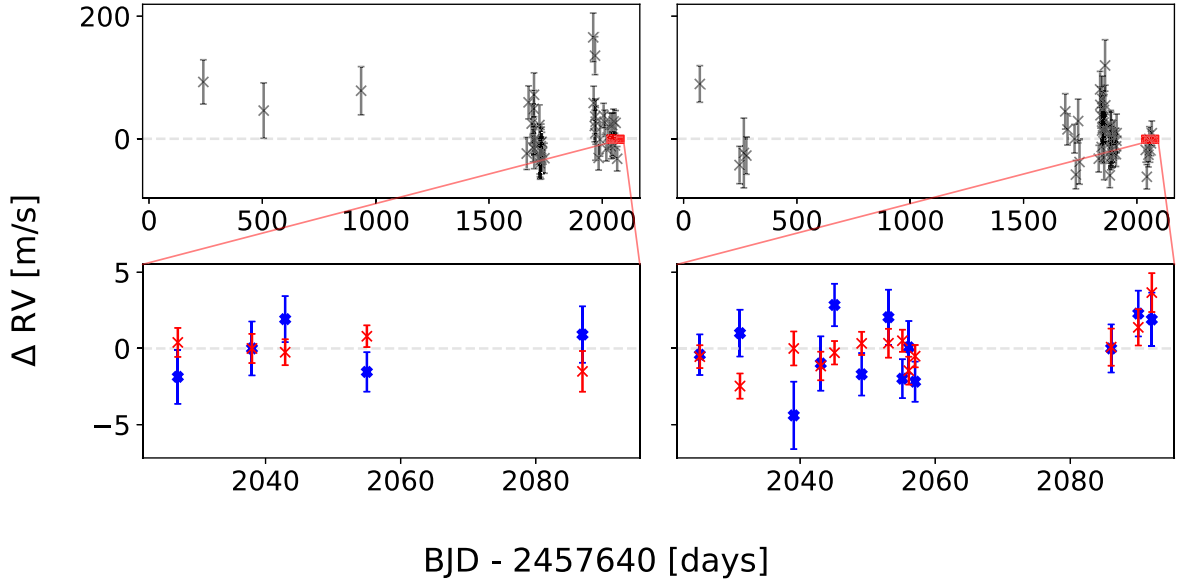
Figure 2. Radial velocity time series for the two candidate variables. The left panels show LHS 2899 and the right panels show G 125-34, while the upper panels show TRES observations and the lower panels show MAROON-X observations. The lower panels cover a much smaller range in time and radial velocity; the overlap is indicated by the red rectangles. Radial velocities from the blue arm of MAROON-X are shown in blue with thick crosses and from the red arm in red with thin crosses. The red arm achieves uncertainties as low as 70 cm s^{-1}. The lack of radial velocity variability in the extreme precision MAROON-X observations refutes all possible orbital solutions consistent with the variability in the TRES data.

MAROON-X team using the SERVAL pipeline (Zechmeister et al. 2018) and are shown in Figure 2. The final observation of LHS 2899 and the final three observations of G 125-34 were taken in a different MAROON-X observing run from the prior observations, with a zero-point offset of -1.5 ± 1.0 m s^{-1} for the blue arm and $+1.5 \pm 1.0$ m s^{-1} for the red arm; the uncertainty in this offset is responsible for the larger error bars for these later observations. The radial velocity time series for both stars are flat at the 1 m s^{-1} level, definitively ruling out all orbital solutions consistent with the TRES data. LHS 2899 and G 125-34 are statistical false positives, with their significance in the TRES follow-up observations likely the result of non-Gaussian outliers. There are no giant planet detections in our 200 star sample.

4.2. Occurrence Rate Constraints

For a given star, j, the probability that we do not detect a planet is $P_{\text{null}}(\mu)_j = 1 - \mu \times C_j$, where μ is the planetary occurrence rate in a given bin and C is the survey completeness in that bin. The probability that we do not detect any planets around any of our stars is then the product:

$$P_{\text{null}}(\mu) = \prod_j (1 - \mu C_j). \qquad (6)$$

To determine a 95% confidence limit on the occurrence rate, we numerically solve for μ given that $P_{\text{null}}(\mu) = 0.05$. While we use this form of the equation to generate our Figure 3, note that in the limit where the binomial approximation $(1 - \mu)^{C_j} \approx 1 - \mu C_j$ applies (i.e., where $\mu < 1$ and $\mu C_j \ll 1$, which is appropriate for this study), this equation can be rewritten as $P_{\text{null}}(\mu) = (1 - \mu)^{N_{\text{eff}}}$, where N_{eff}, the effective sample size, is given by $N_{\text{eff}} = \sum_j C_j$. This form is a convenient simplification, as it only requires the average completeness instead of the completeness for each star in the sample, and it motivates our use of N_{eff} as the color bar axis in this figure.

We conduct an injection and recovery analysis to determine C as a function of $M_P \sin i$ and orbital period. We derive our occurrence rate constraints under the assumption of circular orbits, following the precedent of past works (e.g., Howard et al. 2010b; Mayor et al. 2011). This assumption has been shown to be reasonable for $e < 0.5$ (Endl et al. 2002; Cumming & Dragomir 2010). While many eccentric cold Jupiters meet this criterion (Buchhave et al. 2018), more highly eccentric giant planets are known (e.g., Robertson et al. 2012; Moutou et al. 2015). Notably, giant planet formation via gravitational instability may produce large orbital eccentricities (Jennings & Chiang 2021). We consider the limitations of the circular orbit assumption in the following section.

We consider 100 periods spaced logarithmically between 10^{-1} and 10^5 days and 100 values of $M_P \sin i$ spaced logarithmically between 10^{-1} and 10^1 M_J. For each mass and period, we generate 100 artificial radial velocity time series for each star using the observation times and radial velocity uncertainties of the real data, drawing phases from a random uniform distribution. For each hypothetical planet, every star is assigned a completeness C between 0 and 1, indicating the fraction of trials in which the simulated observations were variable at the $P(\chi^2) < 1\%$ level. The sample size N_{eff} is the sum of these fractions. This completeness assumes that we would gather sufficient MAROON-X follow-up observations to verify that any signal flagged at $P(\chi^2) < 1\%$ significance is a true planet.

Our injection and recovery results are shown in Figure 3, which also includes the period axis recast in terms of the zero-albedo equilibrium temperature, $T_{\text{eq}} = [L/(16\pi\sigma a^2)]^{1/4}$, and instellation, $S = 4\sigma T_{\text{eq}}^4$. This transformation requires the masses and luminosities of each star; we adopt the masses from Winters et al. (2021), which are based on the K-band relation from Benedict et al. (2016), and estimate the bolometric luminosities from the photometry collated in Winters et al. (2021) and distances from Gaia parallaxes (Gaia Collaboration et al. 2018, 2021; Lindegren et al. 2021). In
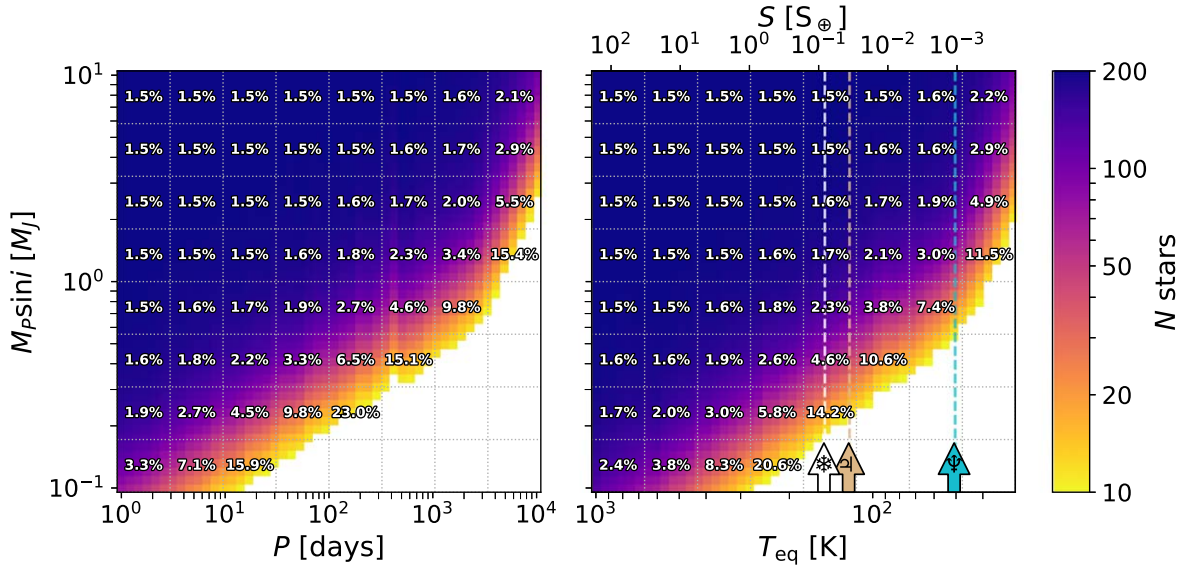
Figure 3. The completeness of our survey, annotated with 95% confidence upper limits on the occurrence rate of giant planets around low-mass M dwarfs as a function of planetary mass and period/instellation/zero-albedo equilibrium temperature under the assumption of circular orbits. In regions where we are highly sensitive (i.e., short periods and large masses), we constrain the occurrence rate to <1.5% with 95% confidence. The color bar indicates N_{eff}, the effective number of stars around which we are sensitive to the hypothetical planet. The arrows in the right-hand plot show instellations equivalent to that of the water snow line (Podolak & Zucker 2004; white), Jupiter (brown), and Neptune (blue). We are sensitive to $M_P \sin i = 1\,M_J$ planets at the water snow line for 83% of stars (occurrence rate < 1.8% with 95% confidence) and at Jupiter-like instellations for 70% of stars (occurrence rate < 2.1%). We remain sensitive to $M_P \sin i = 1\,M_J$ planets at Neptune-like instellations around 19% of stars (occurrence rate < 7.7%).
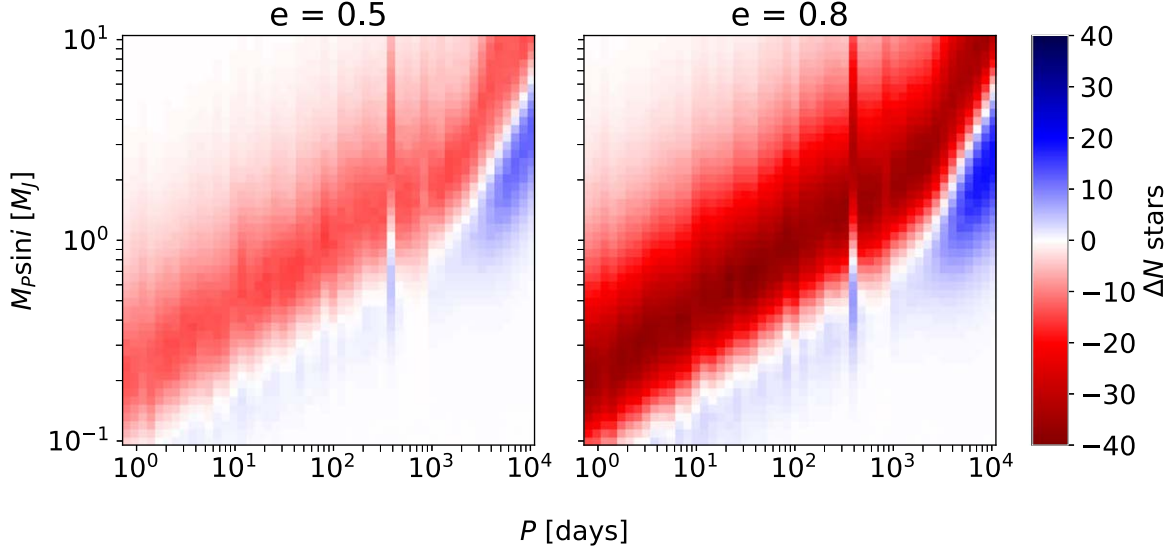
Figure 4. The difference in survey sensitivity between the assumption of circular orbits and the assumption that all planets have $e = 0.5$ (left panel) or $e = 0.8$ (right panel). This difference is given in terms of ΔN_{eff}, the change in the number of stars around which we could detect the planet, with a positive value indicating an increase in the effective number of stars for the eccentric case over the circular case. Given that our total sample contains 200 stars, the circular orbit assumption is generally appropriate for most regions of parameter space; the largest percent decrease in effective sample size is only 13% and 30% for the $e = 0.5$ and $e = 0.8$ assumptions, respectively. There are also previously inaccessible regions of parameter space to which we gain sensitivity when considering eccentric planets (in particular, the regime of super-Jupiters on wide orbits).

particular, we consider the bolometric corrections from both Pecaut & Mamajek (2013) and Mann et al. (2015), adopting the average of the luminosities calculated from these two methods. These masses and luminosities are included in Table 2.

There are two regimes in Figure 3, with a transition around $T_{eq} \approx 50$ K. At short periods, the sensitivity is determined by the radial velocity semiamplitude of the orbit. The slope of the transition region between detectable and undetectable planets represents the interplay between the radial velocity semiamplitude and typical radial velocity uncertainties. At long

periods, the sensitivity drops off rapidly due to the finite length of the observing campaign.

4.3. Eccentric Orbits

To quantify the impact of the circular orbit assumption, we repeat the analysis of the previous section but under the assumption that all planets have $e = 0.5$ in one trial or $e = 0.8$ in another. For each simulated planet, we draw the argument of periastron from a random uniform distribution. Figure 4 shows the change in sensitivities compared to the circular orbits case

in terms of ΔN_{eff}, the change in the number of stars around which the planet is detectable. We find that ΔN_{eff} is generally small; the sample size is never decreased by more than 15 stars in the $e = 0.5$ trial and 39 stars in the $e = 0.8$ trial. There are other regions of parameter space in which the sample size is increased by similar amounts. Moreover, the percent decrease in effective sample size does not exceed 13% or 30%, respectively. Even in the limit where all giant planets are highly eccentric, the circular orbit assumption will produce reasonable occurrence rate constraints.

Compared to a planet on a circular orbit, an eccentric planet achieves a higher radial velocity semiamplitude but spends more time at relative radial velocities near zero. As we approach the sensitivity limit from the detectable side, the decreased likelihood of observing the eccentric orbit in a peak/trough renders a previously detectable planet undetectable. As we approach the sensitivity limit from the undetectable side, the increased amplitude of the peaks/troughs renders a previously undetectable planet detectable.

4.4. Summary of Analysis

To summarize the above reduction and analysis, we do not detect any giant planets in our sample of 200 low-mass, inactive M dwarfs. More specifically, our four measurements for each star do not vary in excess of our $P(\chi^2) = 1\%$ detection limit for 198 stars, and we initially flagged the remaining two stars as candidate radial velocity variables. We collected additional observations of these two candidates with TRES, but were unable to establish the provenance of the signals conclusively. We then obtained observations of the two stars using MAROON-X. The MAROON-X radial velocities show no variation at the $1\,m\,s^{-1}$ level over a two month interval, indicating that the candidate variability from the TRES observations are statistical false positives. After refuting these candidates, none of our stars exhibit radial velocity variability that exceeds our detection threshold. Nevertheless, our injection and recovery analysis indicates that we are very sensitive to a variety of giant planets (Figure 3). We can therefore place strong upper limits on the occurrence rate of these planets, as we discuss in the following section. The median mass of stars in our sample is $0.18\,M_\odot$, with a median radial velocity precision of $29\,m\,s^{-1}$ and a median observation baseline of 3.1 yr.

5. Discussion

5.1. Occurrence of Warm Jupiters

As shown in Figure 3, we have nearly complete sensitivity to $M_P \sin i > 1\,M_J$ planets out to the water snow line. In regions of complete sensitivity, we place a 68% confidence upper limit of 0.57% and a 95% confidence upper limit of 1.5%. Jupiter- and super-Jupiter-mass planets interior to the snow line of low-mass M dwarfs are therefore exceedingly rare.

How does this compare to studies of all types of M dwarfs? The Bonfils et al. (2013) sample contains one planet in this regime: Gliese 876 b (Marcy et al. 1998; Delfosse et al. 1998). While that work published their survey sensitivity in specific bins that differ from the one currently under discussion (their Table 11), inspection of their Figure 15 indicates that they are nearly complete across this parameter range, with N_{eff} equal to roughly 96 stars. If the true occurrence rate of such planets around all M dwarfs was equal to our 68% confidence upper

limit of 0.57%, binomial probability yields a 32% chance that Bonfils et al. (2013) would detect one planet in this bin, with a 58% chance of detecting zero and a 10% chance of detecting two or more planets. Our results are therefore in reasonable agreement with Bonfils et al. (2013) without invoking a decrease in warm Jupiter occurrence around low-mass M dwarfs relative to all M dwarfs, although our occurrence constraints are tighter given that our sample is twice as large. We also note that Gliese 876 has a mass of $0.37\,M_\odot$; i.e., while it is more massive than the M dwarfs in our sample, it is not a particularly massive M dwarf. That said, a decrease in warm Jupiter occurrence around low-mass M dwarfs relative to all M dwarfs is also consistent with our data.

Other constraints on the occurrence rate of giant planets around early M dwarfs are available from transit surveys, although they are limited to hot Jupiters and their bins are not as directly comparable to ours due to the observable of these studies being radius, not mass. Gan et al. (2023) found an occurrence rate of $0.27 \pm 0.09\%$ for hot Jupiters around early $(0.45 \leqslant M_* \leqslant 0.65)$ M dwarfs from TESS, with this statistic defined over the ranges $7\,R_\oplus \leqslant R_P \leqslant 2\,R_J$ and $0.8 \leqslant P \leqslant 10$ days. A similar occurrence rate of such planets around our low-mass M dwarfs is fully consistent with our null detection.

5.2. Occurrence of Giant Planets at the Snow Line

Planet formation theories predict an enhancement in giant planet occurrence at the water snow line (Pollack et al. 1996; Ida & Lin 2008; Morbidelli et al. 2015), a phenomenon that has been observed around Sun-like stars; specifically, Fulton et al. (2021) found that giant planet occurrence in the California Legacy Survey of FGKM stars follows a broken power law, with a peak that approximately coincides with the location of the snow line and which represents a factor of 4 increase in occurrence relative to giant planets interior to the snow line. While this sample does contain a small number of M dwarfs, it is dominated by FGK stars, with 83% of the stars in the sample having stellar masses above $0.6\,M_\odot$ and 98% having stellar masses above $0.3\,M_\odot$ (see Figure 4 of Rosenthal et al. 2021).

As an aside, we note that Fulton et al. (2021) do not make specific statements about the occurrence of giant planets at the snow line of their M dwarfs. In their Figure 7, they do present occurrence rates as a function of stellar mass for giant planets that are more massive than Saturn and that orbit between 1–5 au, including a bin for 0.3–0.5 $M_\odot$ M dwarfs. In this bin, they find an occurrence rate of roughly 5%, with the 68% confidence interval ranging from 5% to 12%. However, this 1–5 au bin represents much lower instellations for M dwarfs than for Sun-like stars. Using the scaling relation $a_{snow} = 2.7(M_*/M_\odot)^{1.14}$ au from Childs et al. (2022; adapted from Mulders et al. 2015), the snow line of a $0.4\,M_\odot$ star occurs at 0.95 au and decreases further to 0.68 au for a $0.3\,M_\odot$ star. Therefore, while the 1–5 au bin is centered on the snow line for Sun-like stars, it does not represent the occurrence rate of giant planets at the snow line of M dwarfs. Rather, it represents the occurrence rate of giant planets on wider orbits.

To investigate the occurrence rate of giant planets at the snow line of low-mass M dwarfs in our sample, we consider a bin corresponding to zero-albedo equilibrium temperatures of $100\,K < T_{eq} < 150\,K$, which we subdivide into mass categories of sub-Jupiters ($0.3\,M_J < M_P \sin i < 0.8\,M_J$), Jupiters ($0.8\,M_J < M_P \sin i < 3\,M_J$), and super-Jupiters ($3\,M_J < M_P \sin i < 10\,M_J$). Assuming uniform occurrence in $\log(T_{eq})$ and $\log(M_P \sin i)$

across each bin, our survey yields 95% confidence upper limits of $<1.5\%$ for super-Jupiters, $<1.7\%$ for Jupiters, and $<4.4\%$ for sub-Jupiters in this region. If we combine the sub-Jupiters and Jupiters into a single $0.3\,M_J < M_P \sin i < 3\,M_J$ mass bin, we obtain a 95% confidence constraint of $<2.4\%$. While this latter bin averages over a strong gradient in our survey completeness, Fulton et al. (2021) showed that the assumption of uniform occurrence in $\log(M_P \sin i)$ holds between 0.1 and $3\,M_J$ in their survey of Sun-like stars. This assumption would therefore be well justified if the formation of all giant planets is less efficient around low-mass M dwarfs, but poorly justified if Jupiter analogs are inhibited around low-mass M dwarfs but sub-Jupiter formation remains efficient (which we discuss in Section 5.4).

Our survey indicates that Jupiter analogs—planets with instellations and masses comparable to Jupiter in our solar system—are rare around low-mass M dwarfs. Moreover, if the Fulton et al. (2021) Sun-like star result holds for low-mass M dwarfs (that is, if giant planets are four times more common near the snow line than on interior orbits), our null detection of giant planets in this region implies an even stronger constraint on warm Jupiters than that presented in the previous section. For our Jupiter bin, we find a 68% confidence upper limit of 0.66%. A fourth of this value is 0.17%; of course, it is also possible that the Sun-like occurrence rate distribution does not hold for low-mass M dwarfs, as we discuss in Section 5.4.

How do our findings at and beyond the snow line compare with other works? It is notable that while few giant planets have been detected around low-mass M dwarfs using radial velocities, others have been inferred through microlensing events (e.g., Skowron et al. 2015; Novati et al. 2018; Ryu et al. 2019). However, comparing microlensing and radial velocity statistics is challenging due to the different observables available to each technique. Clanton & Gaudi (2014b) attempted to circumvent these issues by developing a mapping between microlensing and radial velocity parameters that marginalizes over the unknown physical parameters in the microlensing sample. Using these methods, Clanton & Gaudi (2014a) synthesized radial velocity and microlensing surveys to find an occurrence rate of $2.9^{+1.3}_{-1.5}\%$ for M dwarf planets with $P = 10^0$–10^4 days and $1\,M_J < M_P \sin i < 13\,M_J$. For periods less than 10^2 days, their statistics are fully informed by the radial velocity results of Bonfils et al. (2013), with no contribution from the microlensing sample. As discussed in Section 5.1, Bonfils et al. (2013) yield an occurrence rate of 1% (that is, 1/96) for these warm Jupiters; subtracting this from the 2.9% found by Clanton & Gaudi (2014a) implies a roughly 1.9% occurrence rate for $P = 10^2 - 10^4$ days and $1\,M_J < M_P \sin i < 13\,M_J$. Assuming uniform occurrence in $\log(P)$ and $\log(M_P \sin i)$ across the bin, our survey obtains $N_{\rm eff} = 148$ for giant planets in this regime, producing a 68% confidence upper limit of 0.77% and a 95% confidence upper limit of 2.0% (although note that our sensitivity drops precipitously toward the long-period edge of this bin). Given the large uncertainty in the Clanton & Gaudi (2014a) result, the lack of $M_P \sin i > 1\,M_J$ planet detections in our study is not necessarily in tension with their occurrence rate. However, those authors note that their value is actually more like a lower limit on the occurrence rate, as they use lower limits in the $P = 10^2$–10^3 day range where microlensing sensitivity declines, and they claim their findings are consistent with the nearly twice as large measurement of this occurrence rate from Montet et al. (2014), another radial

velocity survey. As these studies focus on more massive M dwarfs (recall that the microlensing lens distribution is centered at $M_* = 0.5\,M_\odot$, while the mean stellar mass in the Bonfils et al. (2013) sample is $0.35\,M_\odot$), our lack of detections of any giant planets beyond the snow line may be indicative of a decrease in cold Jupiter occurrence around low-mass M dwarfs relative to all M dwarfs.

It is difficult to compare our results directly with Montet et al. (2014), as they report their occurrence rate only in the bin $1\,M_J < M_P < 13\,M_J$ out to 20 au. For a $0.2\,M_\odot$ star, 20 au corresponds to a period of 7×10^4 days; our survey is insensitive to planets at such long periods. We have similar difficulty comparing with the Fulton et al. (2021) occurrence rate of 5% for 100–6000 $M_\oplus$ planets that orbit 0.3–0.5 $M_\odot$ M dwarfs between 1 and 5 au; we have no sensitivity to a 100 $M_\oplus$ planet at 5 au. While we could compare with these surveys by assuming a specific function for the distribution of planets, as done in Montet et al. (2014), we argue in Section 5.4 that the population of planets around low-mass M dwarfs likely does not follow the same functional form as around Sun-like stars. Furthermore, a comparison of occurrence rate at fixed a may not be particularly informative, as these distances represent substantially different instellations when comparing between early and late M dwarfs.

5.3. The Influence of Activity

As stellar activity correlates with rotation rate and hence with radial velocity uncertainty, choosing to restrict our analysis to inactive stars does not greatly affect our sensitivity to Jupiter-sized planets at the snow line: we would not have been able to detect such planets around most active stars due to the larger uncertainties.

However, two giant planets have been previously detected around 0.1–0.3 $M_\odot$ stars: LHS 252 b, a 0.46 M_J planet with a 204 day period (Morales et al. 2019) and GJ 83.1 b, a 0.21 M_J planet with a 771 day period (Feng et al. 2020; Quirrenbach et al. 2022). While both of these stars are within 15 pc, we measure their Hα emission to be in excess of our -1 Å cutoff and hence do not include them in our sample. In our four observations, both stars show statistically significant radial velocity variations that are consistent with their published ephemerides; however, our observing cadence is too sparse to establish that activity has not contributed to the significance of these signals. It is intriguing that the only known giant planets around low-mass M dwarfs orbit active stars. Most active stars are rotationally broadened, meaning they have large radial velocity uncertainties and it would be difficult to detect planets, even in the absence of activity-induced radial velocity jitter. There are only 26 active, low-mass M dwarfs without close binary companions in our volume-complete sample that have $v \sin i$ below 3 km s^{-1}, our detection threshold for line broadening. Two out of these 26 are already known to host a giant planet, and we measure $P(\chi^2) < 1\%$ for three out of the 26 (LHS 252, GJ 83.1, and also GJ 1224). In contrast, we do not detect any giant planets for our 200 inactive M dwarfs.

Is there a reason to expect giant planets to occur preferentially around active M dwarfs? A possible mechanism is the age–activity relation. Younger stars are more active (Kiraga & Stepien 2007; Medina et al. 2022) and have higher metallicities on average. There is compelling evidence that giant planets in shorter period orbits are more common around metal-rich stars than metal-poor stars (Santos et al. 2001;

Fischer & Valenti 2005; Fulton et al. 2021; Rosenthal et al. 2022), although the picture is less clear for M dwarfs (Gaidos & Mann 2014). An inactive sample is therefore biased toward older, metal-poor, possibly planet-deficient stars. However, neither GJ 83.1 nor LHS 252 is particularly metal rich, with [Fe/H] estimates of −0.13 and 0.02 dex, respectively (Newton et al. 2015).

5.4. A Different Occurrence Distribution

The planetary occurrence rate is often parameterized as a function of planetary mass and period (e.g., Cumming et al. 2008). As discussed above, Fulton et al. (2021) advocated for a broken power-law parameterization for the giant planets of Sun-like stars. One might hypothesize that the giant planet occurrence function has the same shape around M dwarfs as it does around Sun-like stars, with the entire distribution scaled down by some constant. However, our results suggest that this is not the case. If the activity of the known planet hosts from the previous section is a coincidence, the discrepancy in occurrence rates could instead be explained by the relatively low masses of LHS 252 b and GJ 83.1 b. LHS 252 b would fall in our sub-Jupiter bin, where we place a weaker 95% confidence upper limit of 4.4%. For $0.21\,M_J$ planets like GJ 83.1 b, our sensitivity drops to only a handful of stars in our snow-line installation bin ($N_{eff} = 4$). It may be that while Jupiter analogs are rare around low-mass M dwarfs, lower-mass giant planets still form, in a way that deviates from the uniform distribution in $\log(M_P \sin i)$ found for the giant planets of Sun-like stars. Future surveys with higher sensitivity to 0.1–$0.3\,M_J$ planets beyond the snow line will be necessary to explore this hypothesis.

However, lower-mass giant planets are unlikely to have a Jupiter-like impact on inner terrestrial planets, as Jupiter's migration profoundly shaped our inner solar system (Walsh et al. 2011). For Sun-like stars, a Jupiter-like mass is required to open a gap in the protoplanetary disk, or a Saturn-like mass in regions of low turbulent activity; smaller giant planets only partially open a gap in their disk (Baruteau & Masset 2013), meaning they operate in a different regime of migration and lack Jupiter's capacity to suppress the inward flow of pebbles. While one might intuitively expect this gap-opening mass to decrease for lower-mass stars, the simulations of Sinclair et al. (2020a) indicate that the threshold mass either increases or holds constant with decreasing stellar mass; those authors note that this behavior is the result of disks around lower-mass stars being geometrically thicker due to reduced gravity, yielding increased pressure forces. Lower-mass giant planets around M dwarfs will therefore not open Jupiter-like gaps.

Our results coupled with microlensing studies also hint at differing behavior with installation. While the occurrence of giant planets peaks just beyond the snow line for Sun-like stars (Fulton et al. 2021), we find no giant planets at these installations. Meanwhile, Poleski et al. (2021) analyzed 20 yr of microlensing data to conclude that, on average, every microlensing star hosts a wide-orbit giant planet ($5 < a < 15$ au and $10^{-4} < M_P/M_* < 0.033$); note that the microlensing lens distribution is dominated by M dwarfs (Gould et al. 2010). There have also been reported detections of $>1\,M_J$ planets around low-mass M dwarfs at very wide orbital separations from direct imaging (Gaidos et al. 2022) and disk studies (Curone et al. 2022). These results hint that giant planet occurrence may peak at lower installations around low-mass M

dwarfs as compared to Sun-like stars. Such a distribution could indicate a pathway for giant planet formation governed by processes unrelated to the water snow line, such as disk instability (Boss 2006; Mercer & Stamatellos 2020). Other possible mechanisms to move giant planets to wide orbits include scattering by planet–planet interactions (e.g., Rasio & Ford 1996) or outward migration in resonance (e.g., Crida et al. 2009).

5.5. Notable Systems

For Sun-like stars, Rosenthal et al. (2022) found that 41% of stars with a close-in, small planet also hosted an outer giant, in contrast to a 17.6% occurrence of outer giants overall. We are therefore particularly attentive to the sensitivity curves for the ten stars in our sample with published small planets: GJ 1214 (Charbonneau et al. 2009), GJ 1132 (Berta-Thompson et al. 2015; Bonfils et al. 2018), LHS 1140 (Dittmann et al. 2017; Ment et al. 2019), GJ 1265 & LHS 350 (Luque et al. 2018), LHS 3844 (Vanderspek et al. 2019), LTT 1445A (Winters et al. 2019, 2022; Lavie et al. 2023), GJ 1061 (Dreizler et al. 2020), GJ 1057 (Bauer et al. 2020), and GJ 585 (Harakawa et al. 2022). While we do not have the radial velocity sensitivity to recover these small planets, we can provide constraints on the existence of further out giant planets to inform our understanding of exoplanetary system architectures.

In Figure 5, we show our sensitivity to giant planets around each of these small-planet hosts. For all stars, we are likely to detect a planet that is Jupiter-like in mass and installation, with our sensitivity varying from just under 50% for LHS 350 to nearly 100% for GJ 1061. As we only have four observations of each star, the sensitivity curves are bumpier than the smooth results of Figure 3; for a given star, there are specific periods in which a planet could feasibly evade detection, although these hiding spots are averaged out when we consider the sample as a whole. For the purposes of Figure 5, we have rerun our analysis with 1000 samples in mass and period to allow the nonhomogeneity of the sensitivity curves to be more readily appreciated. While we cannot definitively rule out the existence of a giant planet beyond the snow line for any individual system, Jupiter-analog companions to inner terrestrial planets —i.e., planetary system architectures like our own—cannot be commonplace for low-mass M dwarfs. If 41% of these stars had a planet that was Jupiter-like in mass and installation (a percentage motivated by the outer giant companion occurrence rate around Sun-like stars from Rosenthal et al. 2022), there is a 98% chance we would have detected this planet around at least one of the ten stars. An abundance of lower-mass giant companions beyond the snow line (e.g., $M_P \sin i \leqslant 0.3\,M_J$) is not ruled out by our observations: if all ten stars had a $0.3\,M_J$ planet at the Jovian installation, there is a 78% chance that we would have detected at least one, but this chance drops to 43% when we lower the incidence to 41%.

5.6. Implications for Terrestrial Planets

What does a lack of outer Jovians imply for the inner terrestrial planets in these systems (notably, the only terrestrial planets amenable to atmospheric study for at least the next decade)? While simulations on this topic are beyond the scope of this work, one can look to the large body of literature discussing the impact of Jupiter on the evolution of our own solar system. Models such as Walsh et al. (2011) suggest that
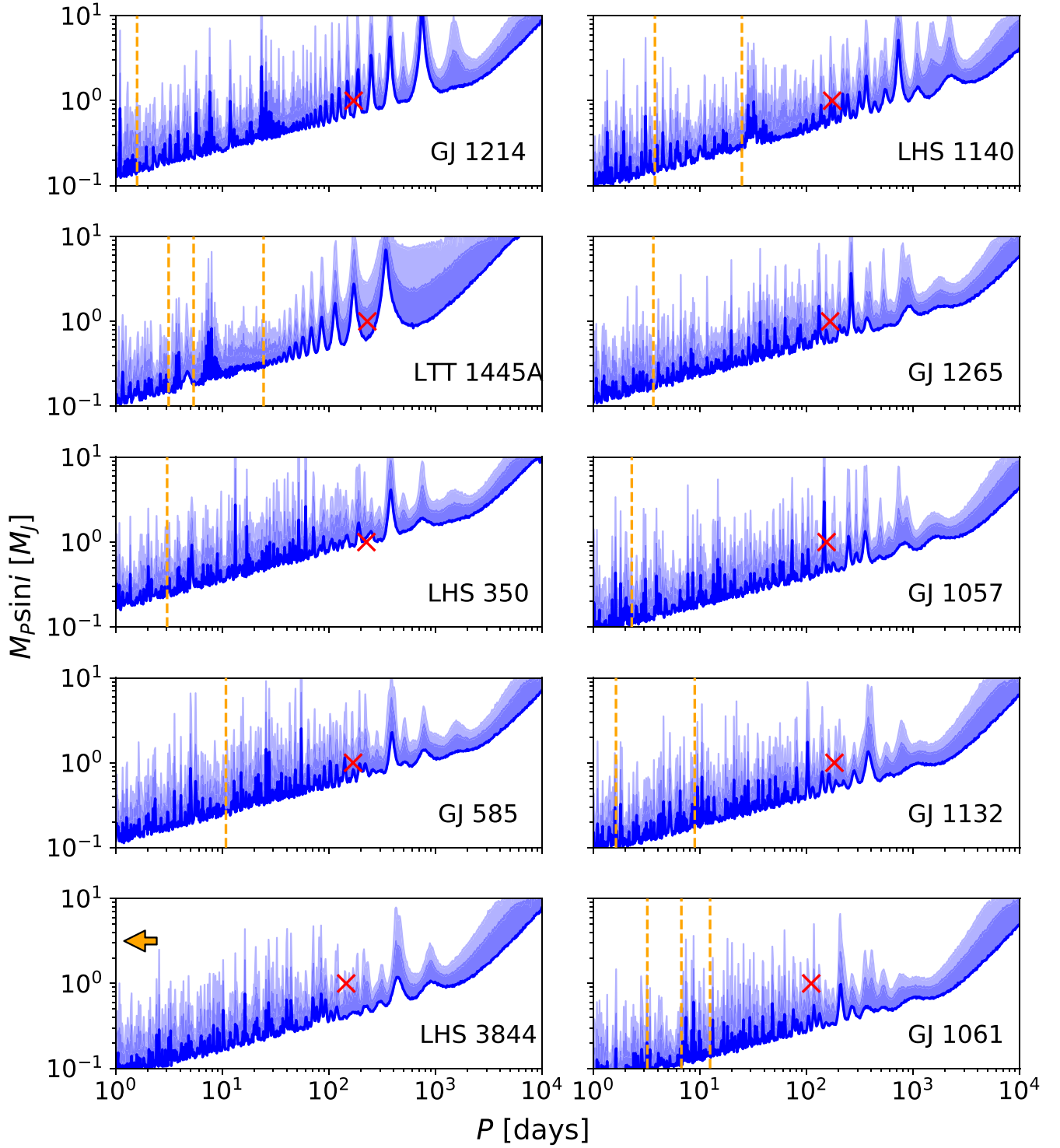
Figure 5. Our sensitivity to giant planets around the ten stars in our survey that are known to host a low-mass planet. The darkest blue line denotes a detection probability of 50%. The contours illustrate where our survey places 84% and 97.5% constraints on the existence of a planet. A hypothetical planet with the instellation and mass of Jupiter is indicated with a red X. Dashed lines show the locations of the known small planets. LHS 3844 b is located off the left edge of the plot.

the migration of Jupiter and Saturn led to the truncation of the planetesimal disk at 1 au, ultimately limiting the size of the terrestrial planets. Meanwhile, Izidoro et al. (2015) suggest that Jupiter acted as a dynamical barrier to the inward migration of gas giant cores, preventing them from migrating into the inner solar system from beyond the snow line and explaining why our solar system lacks a super-Earth (although note Bryan et al. 2019, who found that the presence of super-Earths correlates

positively with the presence of an outer Jovian). Similarly, Bitsch et al. (2021) argue that a Jovian beyond the snow line can block the inward flow of water-rich pebbles, resulting in a drier inner stellar system. Systems without an outer Jovian may therefore have wetter (and potentially, larger) small planets; notably, Luque & Pallé (2022) recently identified a population of water worlds among the small planets that transit M dwarfs (although note Ment & Charbonneau 2023, who found that

volatile-rich small planets are less common around mid-to-late M dwarfs). Giant planets are thought to also set the terrestrial water budget in our own solar system, with Raymond & Izidoro (2017) arguing that Jupiter and Saturn were responsible for delivering Earth's small amount of water through planetesimal scattering.

Childs et al. (2022) note another implication of a lack of outer Jovians: without such a planet, a stellar system is unlikely to have an asteroid belt or a mechanism of delivering asteroids to inner terrestrial planets, and these asteroid impacts may be necessary for the origin of life (e.g., Osinski et al. 2020). Using modeling from Childs et al. (2019), they further argue that lower-mass giant planets (specifically, they replaced Jupiter with a planet of mass $0.14\,M_J$) are unable to sustain suitable asteroid bombardment; more massive giant planets are needed. In the case of Earth, large asteroid impacts are thought to be responsible for the production of a reducing atmosphere (Sinclair et al. 2020b), which ultimately led to the emergence of prebiotic chemistry (Benner et al. 2019).

6. Summary

We present a null detection of giant planets in the volume-complete sample of 200 nearby, inactive 0.10–0.30 $M_\odot$ M dwarfs. We place a 95% confidence upper limit of 1.5% (68% confidence limit of 0.57%) on the occurrence of $M_P \sin i > 1\,M_J$ planets out to the water snow line ($T_{eq} > 150$ K) around these low-mass M dwarfs. At the snow line (100 K < T_{eq} < 150 K), we place 95% confidence upper limits of 1.5%, 1.7%, and 4.4% (68% confidence limits of 0.58%, 0.66%, and 1.7%) for $3\,M_J < M_P \sin i < 10\,M_J$, $0.8\,M_J < M_P \sin i < 3\,M_J$, and $0.3\,M_J < M_P \sin i < 0.8\,M_J$ giant planets, respectively. More granular constraints are given in Figure 3.

Planets that are Jupiter-like in mass and installation are rare around low-mass M dwarfs, consistent with expectations from core accretion theory. Compared with previous radial velocity and microlensing studies that consider broader distributions of M dwarfs with higher mean stellar masses, our results are consistent with a decrease in giant planet occurrence with decreasing M dwarf mass, although direct comparison between surveys is complicated by the limited bins in which occurrence rates have been published and the fact that a given bin in P or a around a more massive star corresponds to a much lower installation around a low-mass M dwarf. In addition, the picture of giant planet occurrence from microlensing is still unclear. If Poleski et al. (2021) are correct in their assertion that every microlensing star has a wide-orbit giant planet, our results imply that the distribution of giant planets around low-mass M dwarfs must differ dramatically from more massive stars, whose giant planets are more prevalent near the water snow line than on wide orbits.

A lack of Jupiter analogs around low-mass M dwarfs has profound impacts for the formation and evolution of habitable-zone terrestrial planets, from their sizes and compositions, to their dynamical environment, to their volatile and refractory budgets, and perhaps to their capacity for life. While terrestrial planets that transit low-mass M dwarfs are promising targets for atmospheric characterization, these worlds will have evolved in a vastly different environment to our own.

ORCID iDs

Emily K. Pass ● https://orcid.org/0000-0002-1533-9029
Jennifer G. Winters ● https://orcid.org/0000-0001-6031-9513
David Charbonneau ● https://orcid.org/0000-0002-9003-484X
David W. Latham ● https://orcid.org/0000-0001-9911-7388
Michael L. Calkins ● https://orcid.org/0000-0002-2830-5661
Gilbert A. Esquerdo ● https://orcid.org/0000-0002-9789-5474
Jessica Mink ● https://orcid.org/0000-0003-3594-1823

References

Apps, K., Clubb, K. I., Fischer, D. A., et al. 2010, PASP, 122, 156
Astropy Collaboration, Price-Whelan, A. M., Sipőcz, B. M., et al. 2018, AJ, 156, 123

Astropy Collaboration, Robitaille, T. P., Tollerud, E. J., et al. 2013, A&A, 558, A33

Bailey, J., Butler, R. P., Tinney, C. G., et al. 2009, ApJ, 690, 743

Baruteau, C., & Masset, F. 2013, in Tides in Astronomy and Astrophysics, ed. J. Souchay, S. Mathis, & T. Tokieda, Vol. 861 (Berlin: Springer), 201

Bauer, F. F., Zechmeister, M., Kaminski, A., et al. 2020, A&A, 640, A50

Bakos, G. Á., Bayliss, D., Bento, J., et al. 2020, AJ, 159, 267

Bayliss, D., Gillen, E., Eigmüller, P., et al. 2018, MNRAS, 475, 4467

Benedict, G. F., Henry, T. J., Franz, O. G., et al. 2016, AJ, 152, 141

Benner, S. A., Bell, E. A., Biondi, E., et al. 2019, arXiv:1908.11327

Berta-Thompson, Z. K., Irwin, J., Charbonneau, D., et al. 2015, Natur, 527, 204

Bertaux, J. L., Lallement, R., Ferron, S., Boonne, C., & Bodichon, R. 2014, A&A, 564, A46

Bitsch, B., Raymond, S. N., Buchhave, L. A., et al. 2021, A&A, 649, L5

Bonfils, X., Almenara, J. M., Cloutier, R., et al. 2018, A&A, 618, A142

Bonfils, X., Delfosse, X., Udry, S., et al. 2013, A&A, 549, A109

Boss, A. P. 2006, ApJ, 643, 501

Bouchy, F., Pepe, F., & Queloz, D. 2001, A&A, 374, 733

Bryan, M. L., Knutson, H. A., Lee, E. J., et al. 2019, AJ, 157, 52

Buchhave, L. A., Bitsch, B., Johansen, A., et al. 2018, ApJ, 856, 37

Buchhave, L. A., Bakos, G. Á., Hartman, J. D., et al. 2010, ApJ, 720, 1118

Butler, R. P., Johnson, J. A., Marcy, G. W., et al. 2006, PASP, 118, 1685

Cañas, C. I., Kanodia, S., Bender, C. F., et al. 2022, AJ, 164, 50

Cañas, C. I., Stefansson, G., Kanodia, S., et al. 2020, AJ, 160, 147

Charbonneau, D., Berta, Z. K., Irwin, J., et al. 2009, Natur, 462, 891

Charbonneau, D., & Deming, D. 2007, arXiv:0706.1047

Childs, A. C., Martin, R. G., & Livio, M. 2022, ApJL, 937, L42

Childs, A. C., Quintana, E., Barclay, T., & Steffen, J. H. 2019, MNRAS, 485, 541

Clanton, C., & Gaudi, B. S. 2014a, ApJ, 791, 91

Clanton, C., & Gaudi, B. S. 2014b, ApJ, 791, 90

Crida, A., Masset, F., & Morbidelli, A. 2009, ApJL, 705, L148

Cumming, A., Butler, R. P., Marcy, G. W., et al. 2008, PASP, 120, 531

Cumming, A., & Dragomir, D. 2010, MNRAS, 401, 1029

Curiel, S., Ortiz-León, G. N., Mioduszewski, A. J., & Torres, R. M. 2020, AJ, 160, 97

Curone, P., Izquierdo, A. F., Testi, L., et al. 2022, A&A, 665, A25

Delfosse, X., Forveille, T., Mayor, M., et al. 1998, A&A, 338, L67

Dittmann, J. A., Irwin, J. M., Charbonneau, D., et al. 2017, Natur, 544, 333

Dreizler, S., Jeffers, S. V., Rodríguez, E., et al. 2020, MNRAS, 493, 536

Endl, M., Kürster, M., Els, S., et al. 2002, A&A, 392, 671

Endl, M., Robertson, P., Cochran, W. D., et al. 2022, AJ, 164, 238

Feng, F., Shectman, S. A., Clement, M. S., et al. 2020, ApJS, 250, 29

Fischer, D. A., & Valenti, J. 2005, ApJ, 622, 1102

Foreman-Mackey, D., Hogg, D. W., Lang, D., & Goodman, J. 2013, PASP, 125, 306

Fulton, B. J., Petigura, E. A., Blunt, S., & Sinukoff, E. 2018, PASP, 130, 044504

Fulton, B. J., Rosenthal, L. J., Hirsch, L. A., et al. 2021, ApJS, 255, 14

Gaia Collaboration, Brown, A. G. A., Vallenari, A., et al. 2018, A&A, 616, A1

Gaia Collaboration, Brown, A. G. A., Vallenari, A., et al. 2021, A&A, 649, A1

Gaidos, E., Hirano, T., Kraus, A. L., et al. 2022, MNRAS, 512, 583

Gaidos, E., & Mann, A. W. 2014, ApJ, 791, 54

Gan, T., Lin, Z., Wang, S. X., et al. 2022, MNRAS, 511, 83

Gan, T., Wang, S. X., Wang, S., et al. 2023, AJ, 165, 17

Gould, A., Dong, S., Gaudi, B. S., et al. 2010, ApJ, 720, 1073

Haghighipour, N., Vogt, S. S., Butler, R. P., et al. 2010, ApJ, 715, 271

Hanuschik, R. W. 2003, A&A, 407, 1157

Harakawa, H., Takarada, T., Kasagi, Y., et al. 2022, PASJ, 74, 904

Harris, C. R., Millman, K. J., van der Walt, S. J., et al. 2020, Natur, 585, 357

Hartman, J. D., Bayliss, D., Brahm, R., et al. 2015, AJ, 149, 166

Howard, A. W., Johnson, J. A., Marcy, G. W., et al. 2010a, ApJ, 721, 1467

Howard, A. W., Marcy, G. W., Johnson, J. A., et al. 2010b, Sci, 330, 653

Hunter, J. D. 2007, CSE, 9, 90

Ida, S., & Lin, D. N. C. 2008, ApJ, 685, 584

Izidoro, A., Raymond, S. N., Morbidelli, A., Hersant, F., & Pierens, A. 2015, ApJL, 800, L22

Jennings, R. M., & Chiang, E. 2021, MNRAS, 507, 5187

Johnson, J. A., Butler, R. P., Marcy, G. W., et al. 2007, ApJ, 670, 833

Johnson, J. A., Gazak, J. Z., Apps, K., et al. 2012, AJ, 143, 111

Johnson, J. A., Howard, A. W., Marcy, G. W., et al. 2010, PASP, 122, 149

Jordán, A., Hartman, J. D., Bayliss, D., et al. 2022, AJ, 163, 125

Kains, N., Street, R. A., Choi, J.-Y., et al. 2013, A&A, 552, A70

Kanodia, S., Libby-Roberts, J., Cañas, C. I., et al. 2022, AJ, 164, 81

Kanodia, S., Mahadevan, S., Libby-Roberts, J., et al. 2023, AJ, 165, 120

Kiraga, M., & Stepien, K. 2007, AcA, 57, 149

Kruijer, T. S., Burkhardt, C., Budde, G., & Kleine, T. 2017, PNAS, 114, 6712

Kurtz, M. J., & Mink, D. J. 1998, PASP, 110, 934

Lam, S. K., Pitrou, A., & Seibert, S. 2015, in Proc. Second Workshop on the LLVM Compiler Infrastructure in HPC, ed. H. Finkel (New York: ACM), 1

Laughlin, G., Bodenheimer, P., & Adams, F. C. 2004, ApJL, 612, L73

Lavie, B., Bouchy, F., Lovis, C., et al. 2023, A&A, 673, 69

Lindegren, L., Klioner, S. A., Hernández, J., et al. 2021, A&A, 649, A2

López-Morales, M., Ben-Ami, S., Gonzalez-Abad, G., et al. 2019, AJ, 158, 24

Lubin, J., Robertson, P., Stefansson, G., et al. 2021, AJ, 162, 61

Lunine, J. I. 2001, PNAS, 98, 809

Luque, R., Nowak, G., Pallé, E., et al. 2018, A&A, 620, A171

Luque, R., & Pallé, E. 2022, Sci, 377, 1211

Mann, A. W., Feiden, G. A., Gaidos, E., Boyajian, T., & von Braun, K. 2015, ApJ, 804, 64

Mann, A. W., Wood, M. L., Schmidt, S. P., et al. 2022, AJ, 163, 156

Marcy, G. W., Butler, R. P., Fischer, D., et al. 2001, ApJ, 556, 296

Marcy, G. W., Butler, R. P., Vogt, S. S., Fischer, D., & Lissauer, J. J. 1998, ApJL, 505, L147

Mayor, M., Marmier, M., Lovis, C., et al. 2011, arXiv:1109.2497

Medina, A. A., Winters, J. G., Irwin, J. M., & Charbonneau, D. 2020, ApJ, 905, 107

Medina, A. A., Winters, J. G., Irwin, J. M., & Charbonneau, D. 2022, ApJ, 935, 104

Ment, K., & Charbonneau, D. 2023, arXiv:2302.04242

Ment, K., Dittmann, J. A., Astudillo-Defru, N., et al. 2019, AJ, 157, 32

Mercer, A., & Stamatellos, D. 2020, A&A, 633, A116

Montet, B. T., Crepp, J. R., Johnson, J. A., Howard, A. W., & Marcy, G. W. 2014, ApJ, 781, 28

Morales, J. C., Mustill, A. J., Ribas, I., et al. 2019, Sci, 365, 1441

Morbidelli, A., Lambrechts, M., Jacobson, S., & Bitsch, B. 2015, Icar, 258, 418

Morley, C. V., Kreidberg, L., Rustamkulov, Z., Robinson, T., & Fortney, J. J. 2017, ApJ, 850, 121

Moutou, C., Curto, G. L., Mayor, M., et al. 2015, A&A, 576, A48

Mróz, P., Udalski, A., Bond, I. A., et al. 2017, AJ, 154, 205

Mulders, G. D., Ciesla, F. J., Min, M., & Pascucci, I. 2015, ApJ, 807, 9

Newton, E. R., Charbonneau, D., Irwin, J., & Mann, A. W. 2015, ApJ, 800, 85

Newton, E. R., Irwin, J., Charbonneau, D., et al. 2017, ApJ, 834, 85

Novati, S. C., Skowron, J., Jung, Y. K., et al. 2018, AJ, 155, 261

Osinski, G. R., Cockell, C. S., Pontefract, A., & Sapers, H. M. 2020, AsBio, 20, 1121

Pass, E. K., Winters, J. G., Charbonneau, D., Irwin, J. M., & Medina, A. A. 2023, arXiv:2306.00799

Pecaut, M. J., & Mamajek, E. E. 2013, ApJS, 208, 9

Podolak, M., & Zucker, S. 2004, M&PS, 39, 1859

Poleski, R., Skowron, J., Mróz, P., et al. 2021, AcA, 71, 1

Pollack, J. B., Hubickyj, O., Bodenheimer, P., et al. 1996, Icar, 124, 62

Quirrenbach, A., Passegger, V. M., Trifonov, T., et al. 2022, A&A, 663, A48

Rasio, F. A., & Ford, E. B. 1996, Sci, 274, 954

Raymond, S. N., & Izidoro, A. 2017, Icar, 297, 134

Robertson, P., Endl, M., Cochran, W. D., et al. 2012, ApJ, 749, 39

Rosenthal, L. J., Fulton, B. J., Hirsch, L. A., et al. 2021, ApJS, 255, 8

Rosenthal, L. J., Knutson, H. A., Chachan, Y., et al. 2022, ApJS, 262, 1

Ryu, Y.-H., Hwang, K.-H., Gould, A., et al. 2019, AJ, 158, 151

Sabotta, S., Schlecker, M., Chaturvedi, P., et al. 2021, A&A, 653, A114

Santos, N. C., Israelian, G., & Mayor, M. 2001, A&A, 373, 1019

Schlecker, M., Burn, R., Sabotta, S., et al. 2022, A&A, 664, A180

Seifahrt, A., Stürmer, J., Bean, J. L., & Schwab, C. 2018, Proc. SPIE, 10702, 107026D

Sinclair, C. A., Rosotti, G. P., Juhasz, A., & Clarke, C. J. 2020a, MNRAS, 493, 3535

Sinclair, C. A., Wyatt, M. C., Morbidelli, A., & Nesvorný, D. 2020b, MNRAS, 499, 5334

Skowron, J., Shin, I.-G., Udalski, A., et al. 2015, ApJ, 804, 33

Snellen, I. A. G., de Kok, R. J., le Poole, R., Brogi, M., & Birkby, J. 2013, ApJ, 764, 182

Tal-Or, L., Zechmeister, M., Reiners, A., et al. 2018, A&A, 614, A122

Tokovinin, A., Fischer, D. A., Bonati, M., et al. 2013, PASP, 125, 1336

Tronsgaard, R., Buchhave, L. A., Wright, J. T., Eastman, J. D., & Blackman, R. T. 2019, MNRAS, 489, 2395

Vanderspek, R., Huang, C. X., Vanderburg, A., et al. 2019, ApJL, 871, L24

Virtanen, P., Gommers, R., Oliphant, T. E., et al. 2020, NatMe, 17, 261

Walsh, K. J., Morbidelli, A., Raymond, S. N., O'Brien, D. P., & Mandell, A. M. 2011, Natur, 475, 206

Winters, J. G., Charbonneau, D., Henry, T. J., et al. 2021, AJ, 161, 63

Winters, J. G., Cloutier, R., Medina, A. A., et al. 2022, AJ, 163, 168

Winters, J. G., Irwin, J. M., Charbonneau, D., et al. 2020, AJ, 159, 290

Winters, J. G., Medina, A. A., Irwin, J. M., et al. 2019, AJ, 158, 152

Zechmeister, M., Reiners, A., Amado, P. J., et al. 2018, A&A, 609, A12

Zucker, S. 2003, MNRAS, 342, 1291